Research Article

Received: 27 July 2026
Accepted: 24 October 2026
Published: 04 November 2026

Design, Modeling, and Experimental Validation of a Novel Flexible-Joint Robotic Manipulator using Adaptive Sliding Mode Control

Hayder Abdalihkwa
Mechanical Engineering Department, College of Engineering, University of Baghdad, Baghdad, Iraq; haidar.zaher2303@coeng.uobaghdad.edu.iq

Waleed Al-Ashtari
Mechanical Engineering Department, College of Engineering, University of Baghdad, Baghdad, Iraq

Cite this article:
H. Abdalihkwa and W. Al-Ashtari (2026). Design, Modeling, and Experimental Validation of a Novel Flexible-Joint Robotic Manipulator using Adaptive Sliding Mode Control. Revista Cultura Científica, (24), pp. 2296–2318. https://doi.org/10.70517/revcc2624187

2026 © The Author(s). Published by Revista Cultura Científica. This article is published as open access under the Creative Commons Attribution 4.0 International (CC BY 4.0) license (http://creativecommons.org/licenses/by/4.0/).

Abstract

This paper presents the design, fabrication, nonlinear dynamic formulation, simulation, and experimental comparison of a robotic manipulator incorporating a four-spring flexible coupling. The platform is described as a four-degree-of-freedom (4-DOF) arm, and the supplied model distinguishes a motor-side coordinate from three load-side coordinates. Conventional sliding-mode control (SMC) and adaptive sliding-mode control (ASMC) are implemented through a LabVIEW real-time environment and a National Instruments myRIO controller. Reported tests consider no added payload, a 1000 g payload, and an external disturbance at reference angles of 45° and 135°. The supplied simulation and experimental summaries are compared using position-error percentages, settling time, and maximum load torque. Across six matched experimental cases, ASMC reduces the reported position-error indicator by 40.4–50.0%, maximum load torque by 11.8–35.4%, and settling time by 4.6–6.3% relative to SMC. These reductions are calculated from the supplied table values and vary with operating condition and reference angle. The author-reported responses indicate recovery following the applied disturbances and less oscillatory behavior with ASMC. However, the available summaries do not quantify complete chattering suppression, statistical variability, or total actuator energy consumption. The adaptive implementation also introduces a smooth switching function, so the respective contributions of adaptation and smoothing are not isolated. The model structure and Lyapunov candidates are presented with explicit limits: the elastic torque law, numerical implementation details, actuator allocation, and complete closed-loop stability derivation require further specification. The comparison therefore supports the reported performance improvements for the investigated cases while identifying the information needed for full reproduction and broader validation.

Keywords: flexible-joint robotic manipulator; adaptive sliding mode control; nonlinear dynamic modeling; experimental validation; four-spring elastic joint; LabVIEW; NI myRIO

1. INTRODUCTION

Flexible-joint robotic manipulators (FJRs) incorporate compliance between an actuator and the driven link. This arrangement can absorb impacts and isolate vibration, making elastic actuation relevant to collaborative robots and other applications requiring controlled mechanical interaction. Nevertheless, compliance alone does not establish the safety or accuracy of a complete robotic system. Studies of joint clearance, elastic prototypes, model predictive control, elastic-structure-preserving control, and recursive dynamics illustrate different ways of addressing the associated mechanical and control problems [1–7]. The defining modeling issue is the separation between motor-side and load-side motion. Their relative displacement stores elastic energy and can generate oscillations that a rigid-joint approximation does not capture adequately. Published work considers nonlinear torsion, passivity, neural control, prescribed performance, disturbance estimation, and constrained predictive control [8–16]. These approaches provide relevant comparisons for a fabricated mechanism, although their assumptions, actuators, and measurement arrangements differ. Experimental studies already exist in this field; the present work therefore concerns the integration and assessment of the particular four-spring mechanism, rather than claiming that physical validation is generally absent from flexible-joint robotics.

Control approaches for FJRs include PID-type and gravity-compensation methods, observer-supported feedback, neural backstepping, prescribed-performance methods, robust adaptive control, and sliding-mode control [17–26]. Conventional sliding-mode control (SMC) is attractive because a properly designed reaching law can accommodate bounded uncertainties and disturbances. Its discontinuous switching action can also excite neglected dynamics or produce high-frequency control activity. A finite sampling interval, measurement noise, actuator dynamics, and saturation affect how that activity appears in hardware. Adaptive and other nonlinear control methods address different aspects of these difficulties [27–30]. The present comparison concerns a fixed-gain SMC implementation and an adaptive switching-gain implementation incorporating a smooth hyperbolic-tangent term. Their performance must be interpreted together: adaptation and smoothing both change the controller, so an improvement cannot automatically be attributed to adaptation alone. The engineering motivation is to examine these implementations on the same fabricated platform under the operating conditions reported by the authors.

This study presents the design, fabrication, nonlinear modeling, simulation, and experimental evaluation of a robotic platform described as having four degrees of freedom (4-DOF), with a four-spring elastic coupling at the principal joint. The springs connect motor-side and load-side flanges to permit relative angular displacement while transmitting torque. A coupled dynamic representation is used to describe the relationship between motor motion and load-side response. Conventional SMC and adaptive sliding-mode control (ASMC) are implemented through a LabVIEW environment and a National Instruments myRIO controller. The resulting comparison focuses on the reported tracking error, settling time, and maximum load torque rather than an independently established optimum. Important implementation details, including the exact elastic torque law and digital control settings, are not fully specified in the supplied description and are identified as reporting limitations.

The investigated operating conditions are no added payload, an added 1000 g payload, and an externally applied disturbance. The tabulated tests use reference angles of 45° and 135°. Numerical and experimental summaries are considered separately before comparing their corresponding trends. The contributions are the description of the fabricated four-spring mechanism, the presentation of a motor–load dynamic formulation, the implementation of the two control approaches on a common real-time platform, and the comparison of the supplied performance summaries. These contributions should be distinguished from a complete validation of every model coefficient, a general proof of closed-loop stability, or a statistically replicated performance assessment. The manuscript provides deterministic summary values; it does not report trial-level data, confidence intervals, or a common quantitative measure of high-frequency chattering.

2. PROBLEM FORMULATION

2.1. PROBLEM STATEMENT

Flexible-joint manipulators can provide mechanical compliance and impact absorption, but the elastic connection introduces a distinction between actuator position and driven-link position. A motor encoder alone therefore need not identify the load angle accurately during acceleration, payload changes, or disturbance recovery. The relative motion can produce transient oscillations, residual positioning errors, and additional demands on the control system. This study addresses these effects through a fabricated compliant joint, a coupled dynamic description, and a comparison of robust control implementations. The purpose of the model is to represent the interaction between motor inertia, transmitted elastic torque, and load-side motion. The following subsections describe the physical platform and the mathematical quantities used in the analysis. The description also distinguishes reported hardware specifications from parameters and implementation details that remain necessary for full reproduction.

2.2. PROPOSED FLEXIBLE-JOINT ROBOTIC MANIPULATOR

The platform was designed and fabricated to investigate the four-spring flexible-joint mechanism, the associated dynamic description, and the control implementations. It comprises a rigid aluminum base, the elastic coupling, and a three-link load-side assembly driven through the reported servo actuators. The four-spring mechanism connects the principal motor-side drive to the first load-side link. The structure is intended to maintain overall support rigidity while allowing elastic deformation at the designated coupling. Figure 1 identifies the assembled robotic arm and the location of the flexible joint. Its role is to document the physical arrangement; it should not be treated as a quantitative measurement of stiffness, damping, or positioning accuracy.

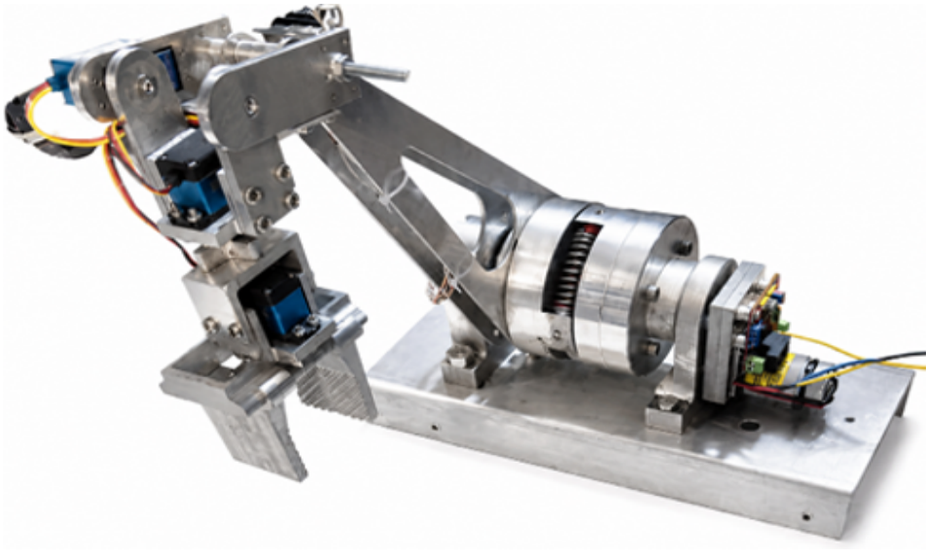


Figure 1. *Robotic Arm With Flexible Joint*

The mechanical components were designed in SolidWorks before fabrication. The geometric models were used to determine nominal dimensions and to support the estimation of component masses and inertia properties for the dynamic description. Nominal CAD properties and measured as-built properties are distinct quantities: machining tolerances, fasteners, wiring, and mounted actuators can change the assembled distribution of mass. The supplied account does not provide a complete identification record for those differences. Consequently, the reported dimensions and masses describe the platform, while the resulting model remains subject to the parameter and measurement limitations discussed below.

1. Base. The aluminum base has nominal dimensions of $380 \times 180 \times 60$ mm and was machined using a computer numerical control (CNC) process. It supports the actuators, flexible-joint assembly, and remaining parts of the robotic arm. Its SolidWorks representation was used during the mechanical design stage to arrange the mounted components.

2. Main Actuator. The main actuator is identified as an ASME-04B DC digital servo motor. It supplies motion to the motor-side flange of the flexible coupling through a commanded angular input. The reported operating-voltage range is 12–24 V DC, with a maximum rated torque of 380 kgf cm, approximately 37.3 N m, at 24 V. This rating is distinct from the maximum load-torque values reported in the performance tables. A rated maximum also does not establish the continuous torque available during a particular experiment. The account does not specify the actuator's internal position-loop dynamics, saturation settings, or the conversion from the external controller output to the servo command; these details affect interpretation of a nominal torque-based control law.

3. Flexible Joint Mechanism. The steel flexible-joint assembly has a nominal cylindrical-frame diameter of 140 mm and comprises two principal flanges. One flange is connected to the motor shaft, and the other is attached to the first load-side link. Four identical springs are arranged symmetrically around the rotational axis between the flanges. Their deformation permits relative rotation and transmits restoring torque. The description establishes the arrangement of the elastic elements, but spring stiffness, attachment geometry, preload, damping, and the permissible deflection range are not numerically specified in the supplied manuscript.

4. Load Side. The load-side assembly is connected to the principal motor through the flexible coupling. It comprises three rigid links and an end-effector, with three DS3135 servo motors reported for the load-side motions. Table 1 summarizes the supplied component descriptions, masses, and nominal lengths. These quantities are retained as reported and should be distinguished from a complete set of inertia tensors, center-of-mass locations, and actuator-transmission parameters required by a fully specified multibody model.

Table 1. *Dimensions And Arrangement Of The Load-side Components*

Part	Description	Mass (g)	Length (mm)
Link 1	Main load-side link after the flexible joint, composed of two connected parts	300	400
Link 2	U-shaped link containing the second servo motor	80	70
Link 3	U-shaped link connected to the gripper rotation motor	80	70
End-effector	Gripper assembly	270	90

2.3. PROPOSED FOUR-SPRING FLEXIBLE JOINT

In a flexible joint, the motor shaft and driven link are connected through an elastic transmission element rather than an ideal rigid coupling. Their angular positions can therefore differ during motion and under external loading. The resulting deformation stores energy and contributes additional dynamic behavior that must be considered in controller design. The proposed mechanism uses four springs distributed symmetrically around the rotational axis, as illustrated in Figure 2. This construction differs physically from a single torsional spring, although an equivalent torsional representation may still be useful if its parameters are identified. Structural symmetry alone does not establish a particular nonlinear stiffness function. The stiffness and torque–deflection relationship depend on spring properties, attachment locations, preload, and the geometry of deformation. The present platform is described as a 4-DOF experimental arm incorporating this elastic coupling; the relationship between that hardware designation and the reduced coordinate vector below requires explicit treatment when reproducing the complete mechanism.

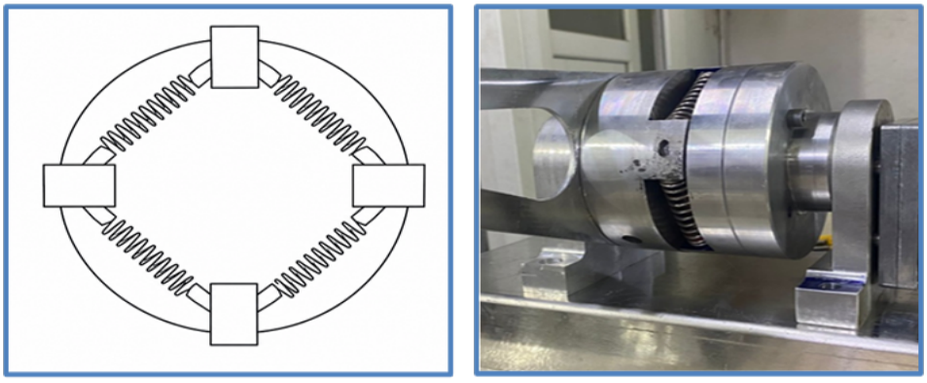


Figure 2. *Four-spring Flexible Joint*

2.4. NONLINEAR DYNAMIC MODEL

The motor angle and the first load-side angle are distinguished because their difference represents deformation at the flexible joint. A control input applied on the motor side must influence the load through that elastic transmission. The model therefore includes motor inertia, load-side dynamics, and the restoring torque generated by the springs. This description is important when interpreting payload effects and transient oscillation. The general matrix form used below does not, by itself, specify all nonlinearities: numerical evaluation requires the mass matrix, velocity-dependent terms, gravity vector, and an explicit elastic torque law. These quantities must be identified consistently with the physical coordinate definitions and actuator arrangement.

Figure 3 presents the intended kinematic configuration, reference frames, and generalized coordinates. The displayed model uses one motor-side coordinate and three load-side coordinates. Joint compliance generally introduces an additional internal coordinate relative to an ideal rigid transmission, so the four-coordinate model must be reconciled with the reported four actuated motions before it can be regarded as a complete model of the whole arm. No undocumented kinematic constraint or omitted actuator coordinate is introduced here. The formulation below is retained as the supplied reduced description, with the mapping between its coordinates and all hardware actuators identified as a limitation. Standard treatments of robot kinematics and elastic-joint dynamics provide the relevant modeling background [11, 31].

The generalized coordinates used in the supplied formulation are collected as

$$q = \begin{bmatrix} \theta_m & \theta_1 & \theta_2 & \theta_3 \end{bmatrix}^T . \tag{1}$$

Here, q is the generalized joint-angle vector, θ_m is the motor-side angle at the elastic coupling, and θ_1, θ_2, and θ_3 are the load-side coordinates represented by the model. Coordinate reference directions must be consistent across the kinematic description, torque distribution, and feedback signals. The elastic relative displacement is associated with $\theta_m - \theta_1$; the precise spring torque produced by that displacement remains to be specified from the mechanism geometry.

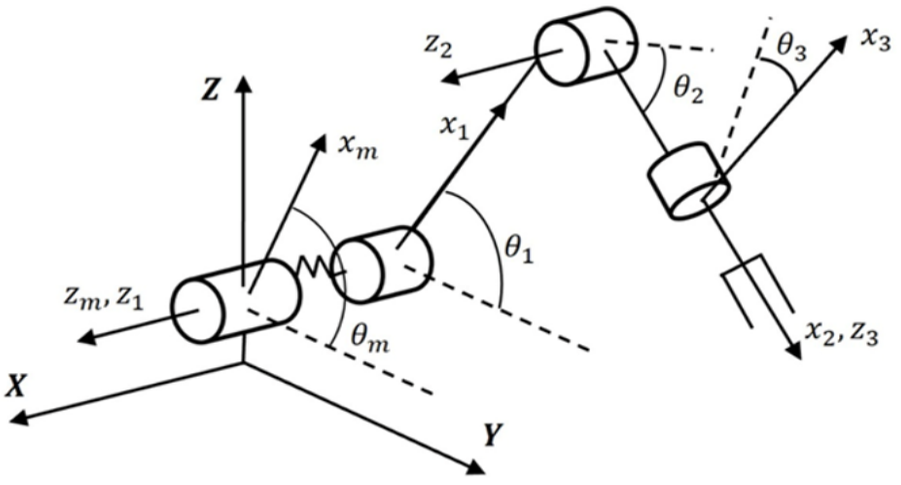


Figure 3. *Kinematic Configuration, Coordinate Frames, And Generalized Coordinates Of The Proposed Flexible-joint Robotic Manipulator*

The total kinetic energy of the system is obtained by combining the kinetic energy of the motor side with the kinetic energies of the three load-side links.

$$K = K_m + \sum_{i=1}^{3} K_i. \tag{2}$$

Similarly, the total gravitational potential energy of the manipulator is expressed as:

$$P_g = \sum_{i=1}^{3} P_i. \tag{3}$$

The Lagrangian for this representation is written in the standard form [31]:

$$\mathcal{L} = K - P_g. \tag{4}$$

In this convention, the spring restoring torque is included explicitly in the generalized force vector below. It must therefore not also be counted through an elastic potential term in the same Lagrangian. An equivalent formulation can include spring potential energy on the left-hand side, but it would then omit the corresponding elastic contribution from the generalized force vector. Stating this convention prevents double counting of the restoring action.

Applying the Euler–Lagrange formulation gives the governing equations for the stated coordinate and force convention [31].

$$\frac{d}{dt}\left(\frac{\partial \mathcal{L}}{\partial \dot{q}_i}\right) - \frac{\partial \mathcal{L}}{\partial q_i} = Q_i, \tag{5}$$

where Q_i is the generalized torque associated with the ith coordinate. Each term has to be evaluated for the same configuration and velocity variables before numerical integration.

The generalized force vector includes the external actuator inputs and the spring torque transmitted between the motor side and the first load-side coordinate. Equal and opposite elastic torques are assigned through

$$B_j = \begin{bmatrix} -1 & 1 & 0 & 0 \end{bmatrix}^T. \tag{6}$$

The direction of T_s is defined consistently with this distribution vector. An explicit constitutive expression for T_s is necessary to calculate the torque generated by the four springs; the matrix B_j only specifies where that torque acts.

Accordingly, the generalized torque vector can be expressed as:

$$Q = \tau_a + B_j T_s. \tag{7}$$

Substituting the generalized force vector into the Euler–Lagrange equations gives the supplied matrix representation:

$$M(q)\ddot{q} + H(q, \dot{q}) + G(q) = \tau_a + B_j T_s. \tag{8}$$

Here, $M(q)$ is the inertia matrix, $H(q,\dot{q})$ contains velocity-dependent terms, and $G(q)$ is the gravitational torque vector. The model requires a nonsingular inertia matrix over the operating region. The external actuator vector is represented as

$$\tau_a = \begin{bmatrix} u & \tau_1 & \tau_2 & \tau_3 \end{bmatrix}^T. \tag{9}$$

The symbol u denotes the principal motor-side control torque, while τ_1, τ_2, and τ_3 denote the remaining modeled actuator inputs. Their association with the coordinates and the three reported load-side servos must be established explicitly. Without that allocation, a matrix equation with matching dimensions is not sufficient evidence that every physical motion has been represented correctly.

For controller implementation and numerical simulation, the nonlinear dynamic model is converted into a first-order state-space representation. The state vector is defined as:

$$x = \begin{bmatrix} x_1 \\ x_2 \\ x_3 \\ x_4 \\ x_5 \\ x_6 \\ x_7 \\ x_8 \end{bmatrix} = \begin{bmatrix} \theta_m \\ \theta_1 \\ \theta_2 \\ \theta_3 \\ \dot{\theta}_m \\ \dot{\theta}_1 \\ \dot{\theta}_2 \\ \dot{\theta}_3 \end{bmatrix}. \tag{10}$$

The corresponding first-order equation is

$$\dot{x} = \begin{bmatrix} \dot{q} \\ M^{-1}(q)\big(\tau_a + B_j T_s - H(q,\dot{q}) - G(q)\big) \end{bmatrix}. \tag{11}$$

The modeled load-side output is selected as

$$y(t) = \begin{bmatrix} \theta_1(t) \\ \theta_2(t) \\ \theta_3(t) \end{bmatrix} = \begin{bmatrix} x_2(t) \\ x_3(t) \\ x_4(t) \end{bmatrix}. \tag{12}$$

The distinction between state and output matters because measurements of motor position alone do not directly provide all the load-side states.

The state-space representation provides a framework for simulation and for interpreting the feedback variables used by SMC and ASMC. Reproduction requires the numerical forms of M, H, G, and T_s, the initial conditions, and the reference trajectories. The supplied manuscript does not include those complete specifications. Accordingly, the formulation is presented as the reported model structure rather than a fully executable or independently validated multibody implementation.

2.5. CONTROLLER DESIGN

SMC and ASMC are considered to improve tracking in the presence of elastic coupling and disturbances. The following equations summarize the control architecture reported for the platform. Lyapunov functions provide a framework for assessing stability, but a stability conclusion requires the complete closed-loop dynamics, consistent input signs, and explicit uncertainty bounds. Those requirements cannot be replaced by selecting a candidate function alone. The description therefore separates the stated controller structure from conditions that would have to be demonstrated in a full proof.

SMC is used to drive a tracking-related sliding variable toward a prescribed surface. Its robust properties depend on the input channel, uncertainty assumptions, switching-gain selection, and the ability of the actuator to realize the command [32]. This qualification is particularly important for a position-controlled servo driven through an external command interface. A torque-level law and an implemented position command are not automatically equivalent unless their mapping and relevant internal dynamics are documented.

The tracking error is defined as

$$e(t) = q_d(t) - q(t), \tag{13}$$

where $q_d(t)$ is the desired coordinate vector and $q(t)$ is the actual modeled coordinate vector. A desired motor-side coordinate must be defined as well as the desired load-side motion when this four-dimensional error vector is used.

The time derivative of the tracking error is expressed as

$$\dot{e} = \dot{q}_d(t) - \dot{q}(t). \tag{14}$$

The sliding-surface vector is selected as [33]

$$S(t) = \dot{e}(t) + \Lambda e(t), \tag{15}$$

with the positive diagonal matrix

$$\Lambda = \mathrm{diag}(\lambda_1, \lambda_2, \lambda_3, \lambda_4), \qquad \lambda_i > 0. \tag{16}$$

The numerical values of the λ_i parameters are necessary for a reproducible assessment of the reported responses.

A conventional candidate for examining the sliding dynamics is [34, 35]

$$V = \frac{1}{2} S^T S. \tag{17}$$

Differentiating with respect to time gives

$$\dot{V} = S^T \dot{S}. \tag{18}$$

The derivative identity follows directly from the candidate definition and does not, by itself, establish negativity or convergence. The effect of the realized input and any uncertainty terms must still be substituted into $\dot{S}$.

A desired reaching condition away from the surface is

$$S^T \dot{S} < 0, \qquad S \neq 0. \tag{19}$$

Showing that this condition holds requires bounds on the relevant disturbances and a compatible control-gain choice. A negative semidefinite derivative alone also requires additional arguments before asymptotic convergence can be concluded.

The reported SMC architecture combines equivalent and switching contributions:

$$u = u_{\mathrm{eq}} + u_{\mathrm{sw}}. \tag{20}$$

Here, u_{eq} denotes the nominal equivalent-control contribution and u_{sw} denotes the switching contribution. These expressions describe the control structure schematically; the complete allocation of a vector sliding signal to the scalar principal input and the remaining servo inputs is not supplied.

The nominal equivalent-control term is associated with the condition

$$\dot{S} = 0, \tag{21}$$

while the switching term is stated as

$$u_{\mathrm{sw}} = -K \,\mathrm{sign}(S). \tag{22}$$

The sign function acts componentwise when S is a vector. The gain and input allocation must have compatible dimensions. The negative sign is retained from the supplied architecture, but its consistency must be checked against the adopted error definition and the sign of the effective input gain. It cannot be assumed to imply the reaching condition independently of the plant dynamics.

For a scalar argument s, the signum function is

$$\mathrm{sign}(s) = \begin{cases} 1, & s > 0, \\ 0, & s = 0, \\ -1, & s < 0. \end{cases} \tag{23}$$

The componentwise vector function applies this definition separately to each sliding component.

Accordingly, the final SMC law is given by

$$u = u_{eq} - K \,\mathrm{sign}(S). \tag{24}$$

The overall closed-loop control system of the proposed SMC controller is shown in Figure 4. The tracking error and the designed sliding surface are fed to the controller, which calculates the control signal and sends it to the nonlinear flexible-joint robotic manipulator via the equivalent and switching control blocks.

A discontinuous switching term can produce high-frequency control activity and excite unmodeled mechanical or actuator dynamics. This is commonly described as chattering, although a quantitative assessment requires suitable signal

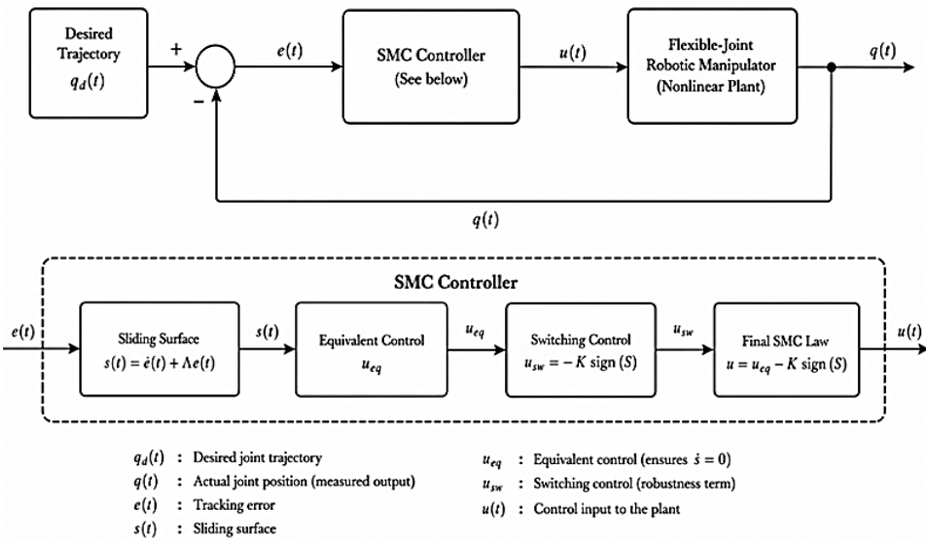


Figure 4. *Block Diagram Of The Proposed SMC*

resolution and a stated measure. The ASMC implementation below changes both the gain adaptation and the switching function. It is intended to smooth the response while retaining disturbance compensation within the operating conditions tested; the available summary tables do not establish complete elimination of chattering.

The selection of a fixed switching gain involves a trade-off. A small gain may not dominate uncertainty, while a large gain can increase unnecessary control activity. The adaptive structure is intended to adjust the switching magnitude during operation [36, 37]. The following adaptation equations are written for a single scalar sliding component, denoted by s, to distinguish them from the vector surface S. A multichannel implementation would need a documented rule for applying the scalar gains or a consistently defined vector adaptation law. The supplied description does not specify that allocation.

For the scalar sliding channel, the reported smoothed switching contribution is

$$u_{\mathrm{sw}} = -\eta(t)\tanh\left(\frac{s}{\phi}\right), \tag{25}$$

where $\eta(t)$ is an adaptive switching gain and $\phi > 0$ specifies the smoothing scale. The hyperbolic tangent replaces the discontinuous sign function with a continuous approximation. Its slope near the origin depends on ϕ, so the boundary-layer choice affects both smoothness and residual tracking behavior.

The scalar ASMC architecture is consequently written as

$$u = u_{\mathrm{eq}} - \eta(t)\tanh\left(\frac{s}{\phi}\right). \tag{26}$$

As for the SMC expression, the input sign and the conversion to the physical servo command must be established from the implemented plant and feedback arrangement.

The stated scalar gain update is

$$\dot{\eta} = \gamma|s|, \qquad \gamma > 0. \tag{27}$$

This law is nondecreasing because its right-hand side is nonnegative. It does not include gain reduction, leakage, projection, or an upper bound. Therefore, smoother switching cannot be attributed to a gain that necessarily decreases near the surface. Initial gain, adaptation rate, smoothing scale, sampling period, and any implemented gain limits need to be reported separately.

Figure 5 presents the reported ASMC architecture. The adaptive gain modifies the magnitude of the switching contribution, while the hyperbolic-tangent function smooths its variation with the sliding signal. These mechanisms have different effects and should be distinguished when interpreting a comparison with fixed-gain discontinuous SMC. No additional gain-tuning rule is assumed beyond the update stated in Eq. (27).

For a scalar channel, an augmented Lyapunov candidate can be written in the reported form [35]:

$$V = \frac{1}{2}s^2 + \frac{1}{2\gamma}(\eta - \eta^*)^2, \tag{28}$$

where η^* is a constant reference bound used in the analysis. Its relationship to the lumped uncertainty must be defined for a stability argument. It is not a measured parameter established by the performance tables.

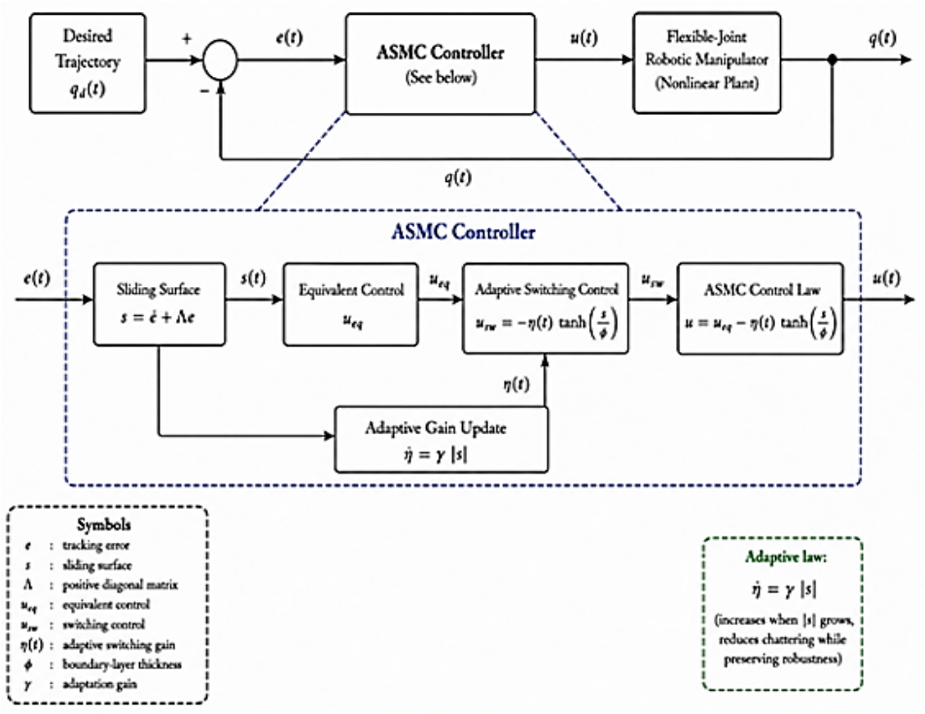


Figure 5. *Block Diagram Of The Proposed ASMC*

Taking the time derivative of the Lyapunov function yields:

$$\dot{V} = s\dot{s} + \frac{1}{\gamma}(\eta - \eta^*)\dot{\eta}. \tag{29}$$

A full analysis would substitute the actual closed-loop sliding dynamics and the adaptation law in Eq. (27) into Eq. (29), and then establish the required inequality

$$\dot{V} \leq 0. \tag{30}$$

The supplied equations do not provide the explicit equivalent control, uncertainty bound, effective input gain, or complete actuator mapping needed to demonstrate that inequality. In addition, smoothing the switching function changes the reaching behavior within its boundary layer. The inequality is therefore identified as an analytical requirement rather than asserted as an already completed proof.

The experimental and simulation responses can be assessed for tracking and disturbance recovery without claiming a general asymptotic-stability theorem from the incomplete derivation. Boundedness, ultimate tracking accuracy, and asymptotic convergence are distinct conclusions and require different conditions. A proof would need to address the servo dynamics, possible saturation, measurement processing, and the invariant or limiting set associated with the selected Lyapunov candidate. The reported response summaries support a restricted comparison under the investigated conditions; they do not establish guaranteed stability for every trajectory, payload, disturbance, or controller parameter choice.

3. RESULTS AND DISCUSSION

The reported evaluation combines numerical simulation and experiments on the fabricated platform. SMC and ASMC were compared under no added payload, a 1000 g payload, and an externally applied disturbance, using reference positions of 45° and 135°. The performance summaries comprise angular position error, settling time, and maximum load torque. These numerical values are retained as supplied by the authors. References concerning flexible-joint control provide methodological context but are not evidence for the present experiment's measurements. Relative improvements are calculated from matched rows of the experimental tables. This distinction separates the source measurements from the arithmetic used to summarize their differences.

3.1. SIMULATION RESULTS

Both controllers were reportedly simulated under matching reference-angle and loading conditions. The numerical comparison concerns the effects of the fixed and adaptive switching implementations on tracking and the reported torque response. The simulation tables can be compared directly at each reference angle, but exact reproduction also requires the integration method, solver tolerances, initial states, elastic parameters, controller gains, and disturbance definition. Those

settings are not fully included in the supplied account. Consequently, the numerical summaries are interpreted as the reported outcomes for this model implementation, rather than as a fully independently reproducible simulation package.

The conventional SMC results provide the reference for the controller comparison. Its intended action is to drive the sliding variable toward the selected surface despite uncertainties, although the realized response depends on the plant and switching implementation. Figures 6 and 7 present the reported simulated motor-side and load-side trajectories under no added payload and a 1000 g payload, respectively. The comparison should distinguish transient elastic oscillation from steady tracking error. It should also distinguish a time-domain response that appears smooth at the plotted scale from a quantified reduction in high-frequency switching activity.

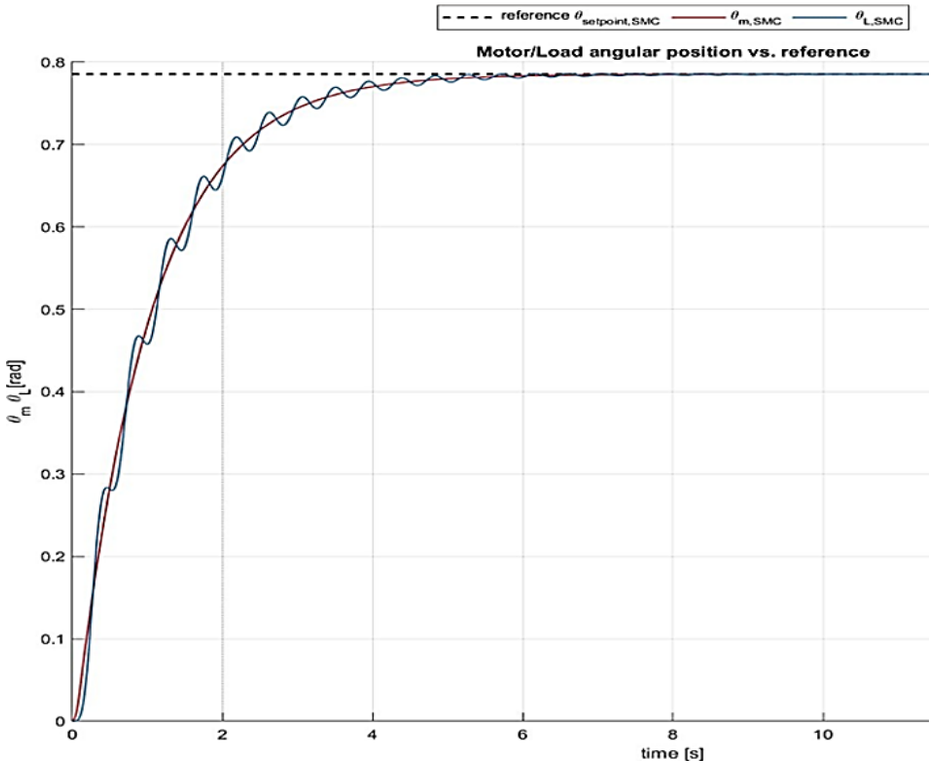


Figure 6. *Simulated Response Of The SMC Controller Under No-load Condition*

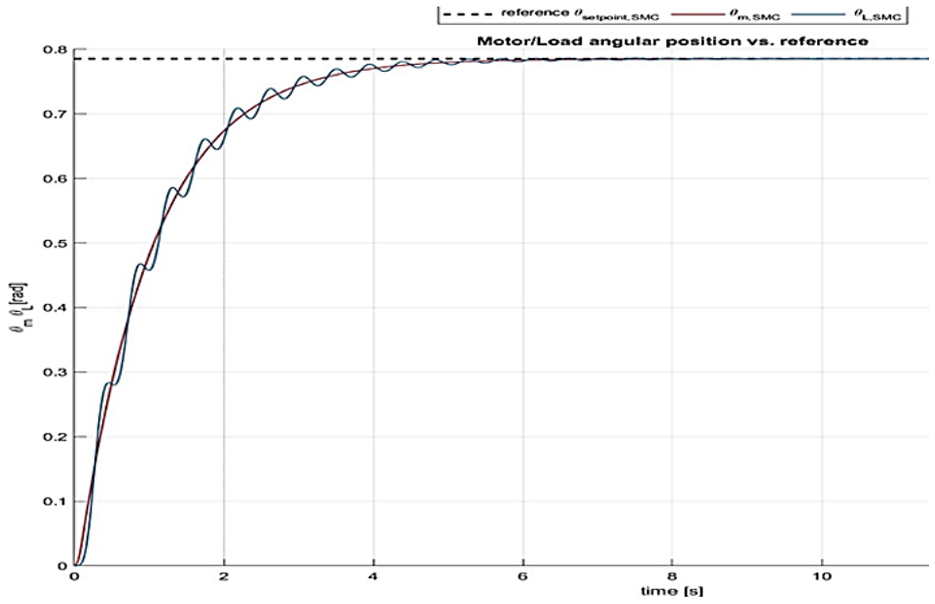


Figure 7. *Simulated Response Of The SMC Controller Under A 1000 g Payload*

The reported trajectories in Figures 6 and 7 show transient motor–load differences followed by settling toward the reference. Joint compliance permits relative angular motion, so a difference between the two responses is physically expected during acceleration and loading. The additional payload changes both inertial and gravitational demands. The

author-reported settling behavior is consistent with a stabilizing response in those simulated cases, but does not establish a general stability result. The corresponding numerical quantities in Tables 2 and 3 provide a more explicit basis for comparing the supplied outcomes.

Figure 8 presents the reported SMC response after a disturbance was applied once the system had settled. The motor-side and load-side positions are described as deviating temporarily and then recovering toward the command. This test assesses disturbance recovery for the particular simulated perturbation; it does not establish a universal robustness margin. The disturbance time history and its relationship to the experimental perturbation need to be specified before the numerical and physical responses can be compared under an identical input.

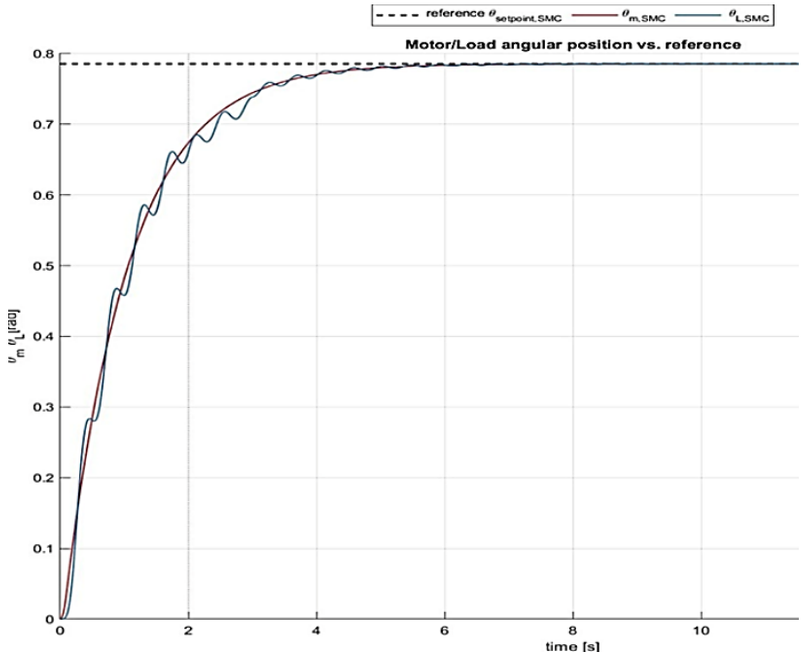


Figure 8. *SMC Controller With A 1000 g Payload And An External Disturbance*

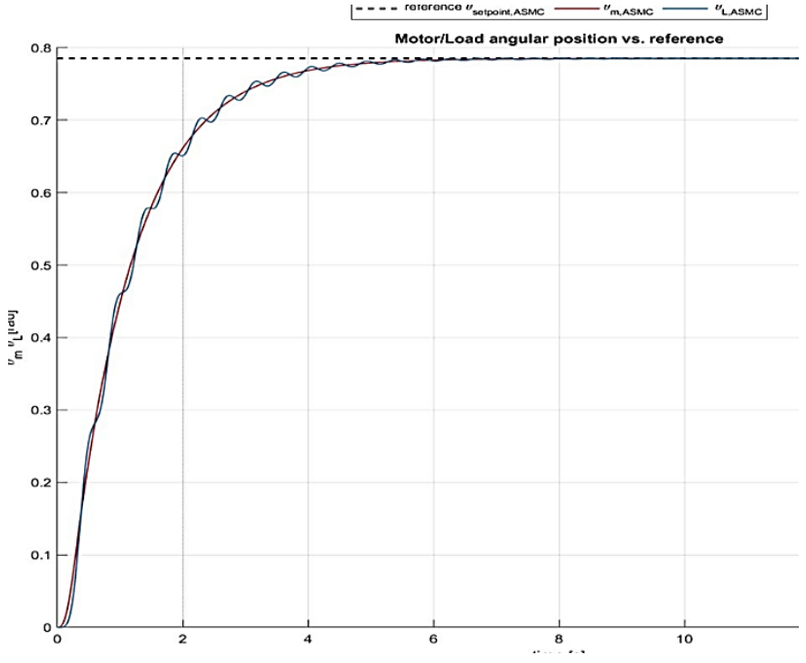


Figure 9. *ASMC Controller Under No-load Condition*

The ASMC comparison changes the fixed discontinuous switching contribution to an adaptive, continuously smoothed contribution. Its purpose is to reduce unnecessary oscillatory activity while retaining useful disturbance compensation. The reported no-load, payload, and disturbance trajectories are considered under the same categories as those used for SMC. Because gain adaptation and the hyperbolic-tangent approximation are introduced together, a separate fixed-gain

smoothed controller would be needed to isolate their individual contributions. No such additional comparison is reported in the supplied results.

Figure 9 presents the reported no-load ASMC response. The description indicates reduced motor–load oscillation and convergence toward the command at the plotted scale. That observation is compatible with a smoother transient response. It does not independently quantify switching frequency, torque ripple, or actuator wear, and the absence of a stated chattering metric limits a stronger claim about complete suppression.

Figure 10 presents the ASMC response with an added 1000 g payload. The reported trajectory shows a change in transient behavior while retaining convergence toward the reference. The additional payload affects the load-side inertia and gravity torque, and the elastic deflection can therefore differ from the no-load case. ASMC denotes adaptive sliding-mode control; its performance here is interpreted through the supplied response and summary values rather than through a different control architecture.

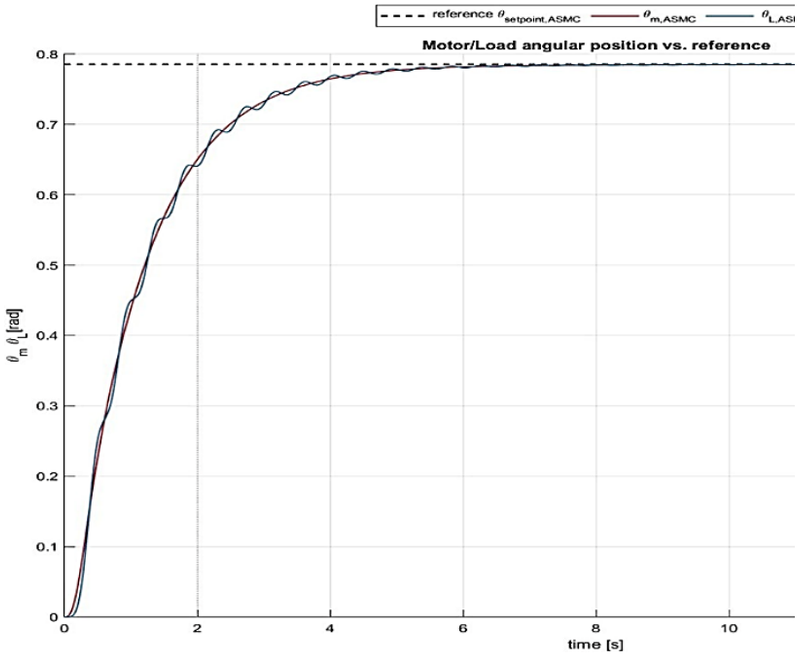


Figure 10. *ASMC Controller Under A 1000 g Payload*

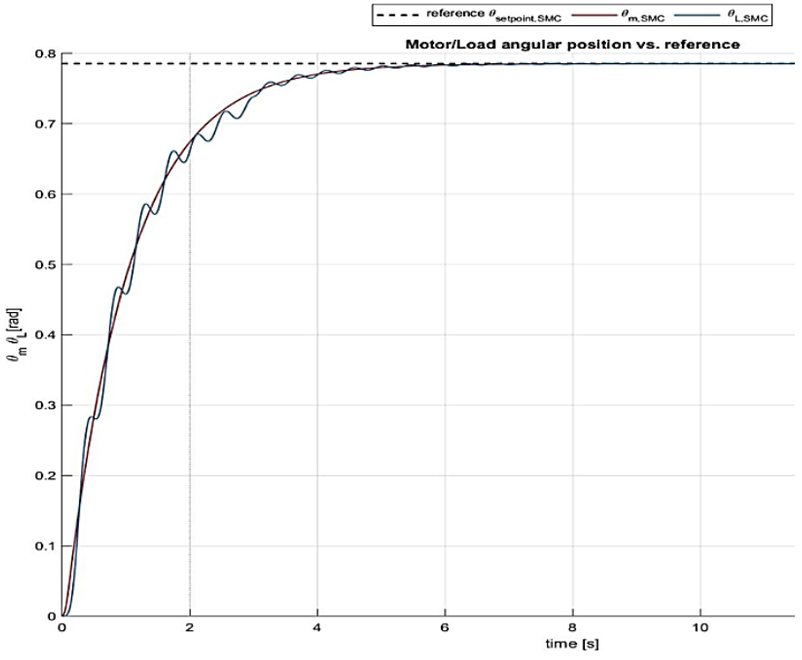


Figure 11. *Response Of The ASMC Controller Under A 1000 g Payload With An External Disturbance*

Figure 11 presents the reported ASMC response to an external disturbance under the loaded condition. The trajectory is

described as showing a transient deviation followed by attenuation of oscillations and recovery toward the reference. This is evidence of disturbance recovery in the reported case. Disturbance amplitude, duration, direction, application point, and injection time are required to compare robustness quantitatively across implementations; those specifications are not fully provided.

Figures 12 and 13 compare the author-reported torque responses for no added payload and the 1000 g payload. The ASMC traces are described as less oscillatory, with lower peaks than the conventional SMC traces. The tables support a comparison of maximum reported load torque, while the shape of a torque signal would require the original time series for independent assessment. A lower maximum does not by itself demonstrate lower total energy consumption, RMS torque, or thermal loading. Those quantities depend on the signal over time, the actuator characteristics, and the motion duration. The results are therefore described in terms of the performance indicators actually supplied, without treating peak torque as a complete measure of control effort.

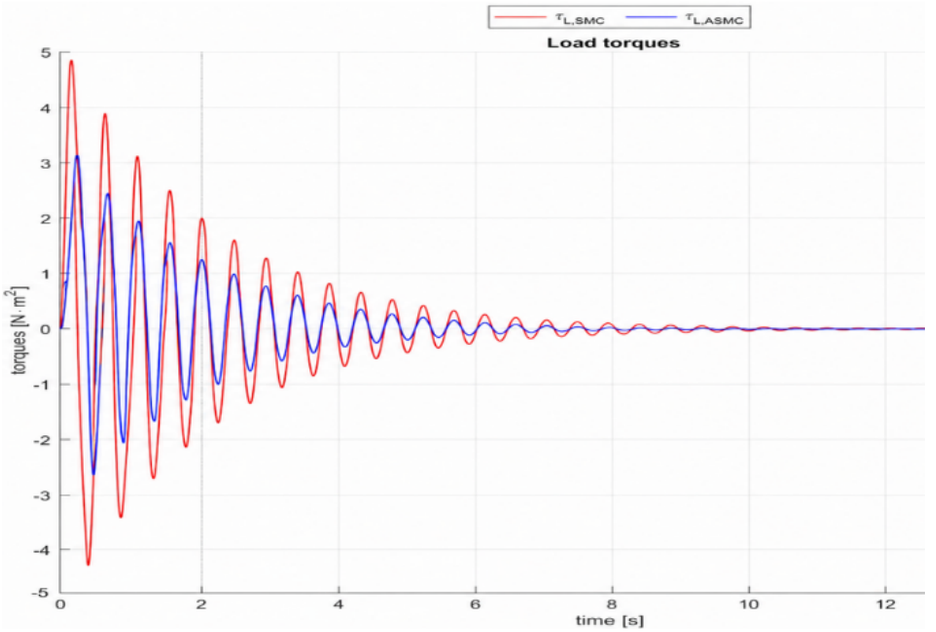


Figure 12. *Comparison Of SMC And ASMC Controller Torque Under No-load Condition*

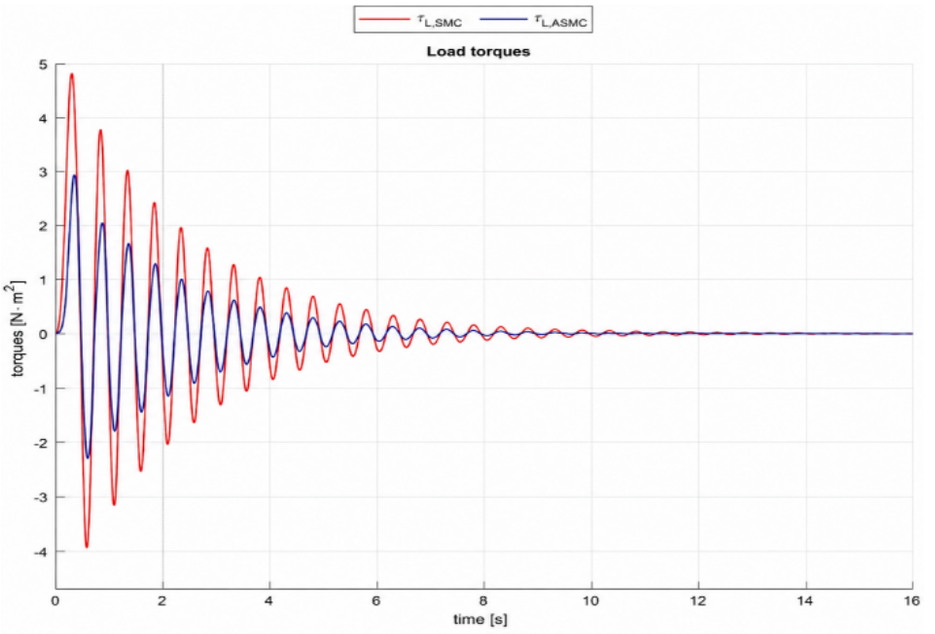


Figure 13. *Comparison Of Load Torque With 1000 g Under SMC And ASMC Controllers*

Following the external disturbance, the load torque temporarily increases for both controllers. Nevertheless, the ASMC attenuates the resulting torque oscillations more rapidly than the conventional SMC, demonstrating improved robustness

and a faster recovery to stable operation (Figure 14). Tables 2 and 3 show the simulation performance values of the SMC and ASMC controllers under different conditions.

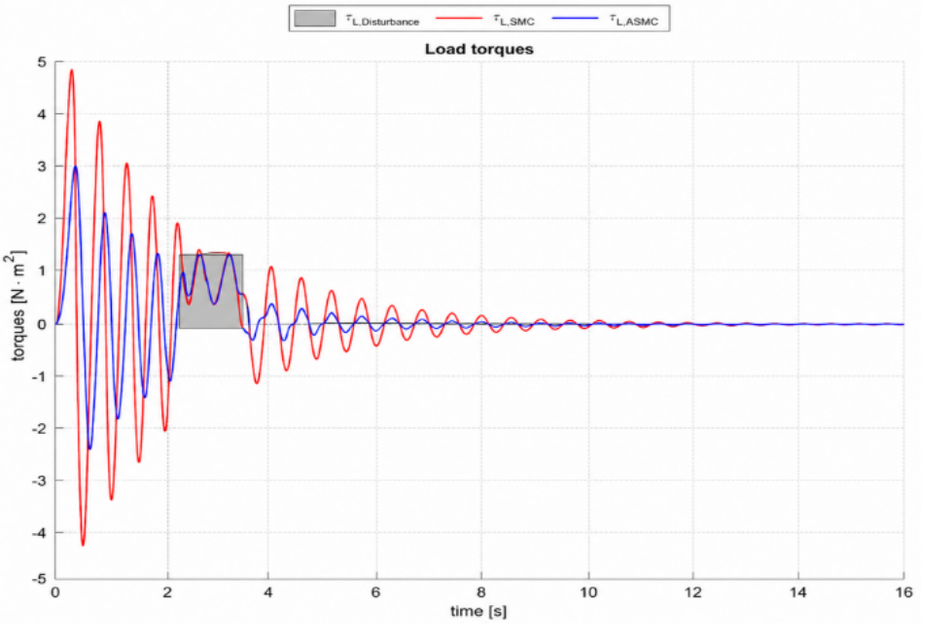


Figure 14. *Comparison Of Load Torque With 1000 g With External Disturbance Under SMC And ASMC Controller Conditions*

Table 2. *Simulation Performance Of The SMC Controller Under Different Conditions*

Reference Angle	Operating Condition	Settling Time (s)	Position Error (%)	Maximum Load Torque (N m)
45°	No-load	5.5	0.72	4.85
45°	1000 g Payload	5.7	0.95	4.90
45°	External Disturbance	5.9	1.35	5.2
135°	No-load	5.6	0.68	5.2
135°	1000 g Payload	5.9	0.9	5.85
135°	External Disturbance	6.1	1.28	6.25

Table 3. *Simulation Performance Of The ASMC Controller Under Different Operating Conditions*

Reference Angle	Operating Condition	Settling Time (s)	Position Error (%)	Maximum Load Torque (N m)
45°	No-load	5.3	0.38	3.12
45°	1000 g Payload	5.5	0.52	3.15
45°	External Disturbance	5.6	0.74	3.45
135°	No-load	5.4	0.34	3.4
135°	1000 g Payload	5.7	0.48	4.45
135°	External Disturbance	5.9	0.69	4.8

3.2. EXPERIMENTAL RESULTS

The experimental evaluation was conducted on the developed four-degree-of-freedom flexible-joint robotic manipulator using the LabVIEW real-time control environment and the National Instruments myRIO platform. The SMC and ASMC controllers were tested under no-load, 1000 g payload, and externally applied disturbance conditions. The experimental responses were assessed in terms of angular position tracking, tracking error, reported load torque, settling time, and disturbance rejection capability. Figure 15 presents the experimental flexible-joint robotic manipulator carrying a 1000 g payload during the experimental evaluation.

The conventional SMC implementation was tested under the same categories of operating conditions used for the numerical comparison. The experimental description concerns the motor-side and load-side position responses and the reported torque indicator. The supplied account does not identify a calibrated torque transducer or provide the calculation used to obtain the tabulated load torque. Accordingly, those values are retained as reported maximum load torques, without relabeling them as independently measured motor torque.



Figure 15. *Experimental Setup Of The Proposed Flexible-joint Robotic Manipulator*

Figures 16 and 17 present the reported experimental SMC trajectories under no added payload and a 1000 g payload. The no-load description indicates a transient oscillation followed by settling near the command. With the payload, the reported response has a larger motor–load difference and more pronounced transient motion. These differences are compatible with the additional inertial and gravitational demands acting through the elastic joint. Both trajectories are described as approaching the reference after the transient. The comparison supports an assessment of the recorded cases, but its interpretation depends on the unreported details of signal filtering, reference generation, and repeatability. In particular, a response that settles during a finite test should not be used as a substitute for the analytical closed-loop conditions discussed above.

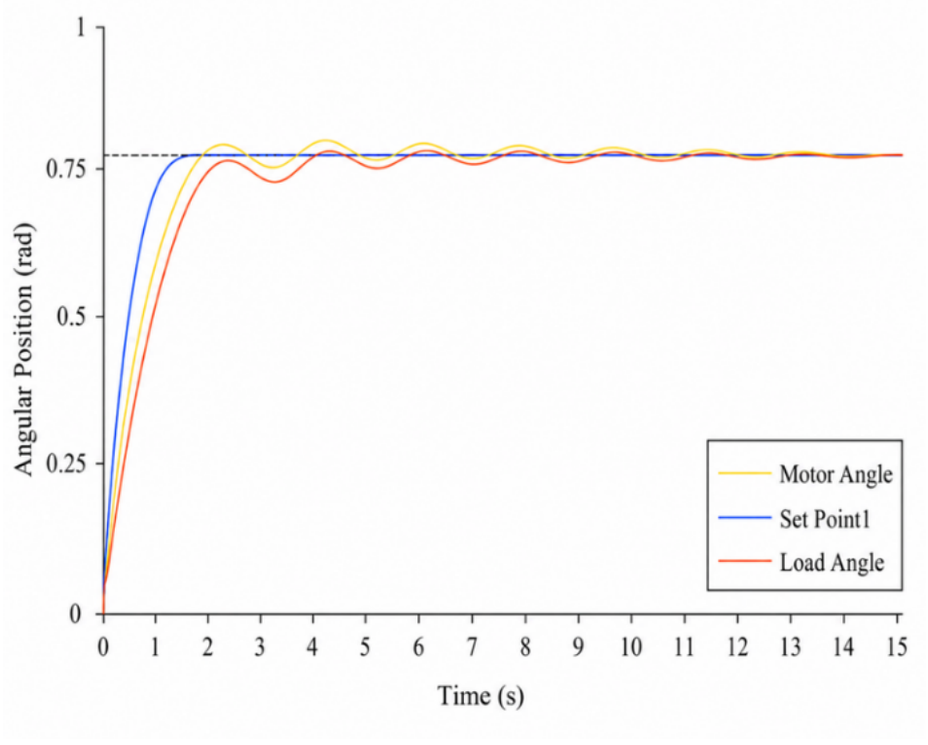


Figure 16. *Experimental Response Of The SMC Controller Under The No-load Condition*

The experimental disturbance case for conventional SMC is presented in Figure 18. The reported positions temporarily deviate from the reference and subsequently recover as the oscillations attenuate. This behavior indicates recovery under the applied disturbance used in that test. The magnitude and time history of that disturbance are not stated, so the result cannot establish a numerical rejection bound or a maximum tolerable perturbation. Table 4 records the supplied SMC settling times, position-error percentages, and maximum load torques for the three operating-condition categories at both reference angles. The category labeled external disturbance is discussed in the text and captions as a loaded disturbance case; the exact payload and disturbance protocol should be confirmed from the experimental record.

Initially, the performance of the ASMC was experimentally evaluated under the no-load condition with a 45° set point, followed by a 1000 g payload test to examine the effect of the applied load on the tracking performance.

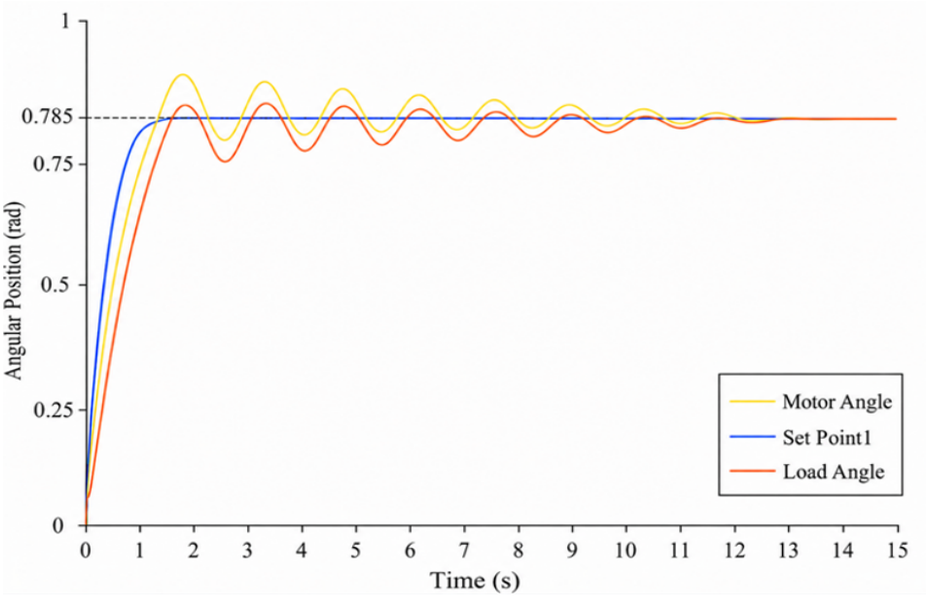


Figure 17. *Experimental Response Of The SMC Controller With A 1000 g Condition*

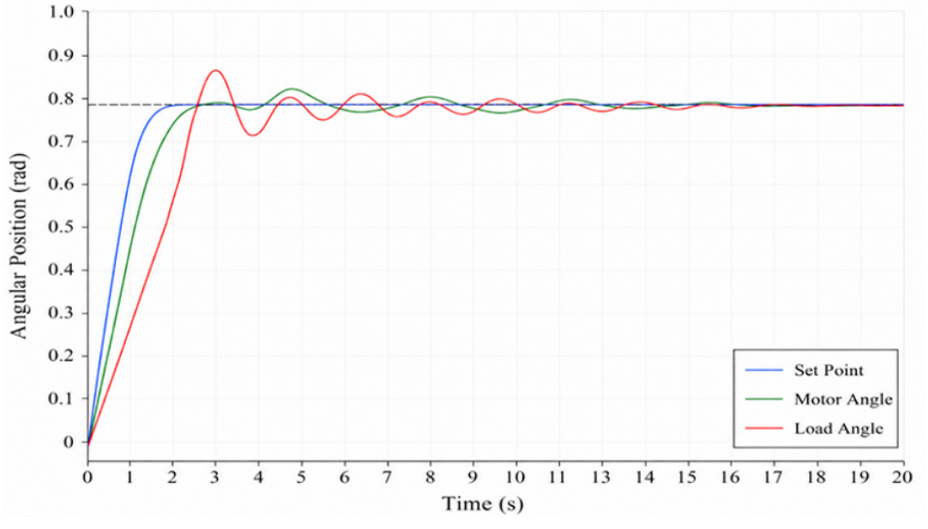


Figure 18. *Experimental Response Of The SMC With A 1000 g Payload And External Disturbance*

Table 4. *Experimental Performance Of SMC Under Different Conditions*

Reference Angle	Operating Condition	Settling Time (s)	Position Error (%)	Maximum Load Torque (N m)
45°	No-load	5.8	1.12	4.86
45°	1000 g Payload	6.0	1.42	4.92
45°	External Disturbance	6.3	2.08	4.95
135°	No-load	5.9	1.08	5.18
135°	1000 g Payload	6.2	1.38	5.82
135°	External Disturbance	6.5	1.98	6.18

As shown in Figure 19, under the no-load condition, both the motor-side and load-side positions rapidly approach the desired reference position of approximately 0.785 rad. A small transient overshoot and oscillatory response can be observed due to the flexibility of the joint; however, these oscillations gradually attenuate, and both responses converge toward the reference position with stable steady-state behavior. When a 1000 g payload is introduced, Figure 20 shows that the ASMC maintains stable position tracking despite the additional inertial and gravitational effects associated with the payload. Compared with the no-load condition, the loaded response exhibits larger transient oscillations and a greater difference between the motor-side and load-side positions. Nevertheless, the oscillations gradually decrease in amplitude, and both responses converge toward the desired reference position. These results demonstrate that the ASMC maintains closed-loop stability and satisfactory position-tracking performance under both no-load and 1000 g payload conditions, despite the increased dynamic effects introduced by the applied payload.

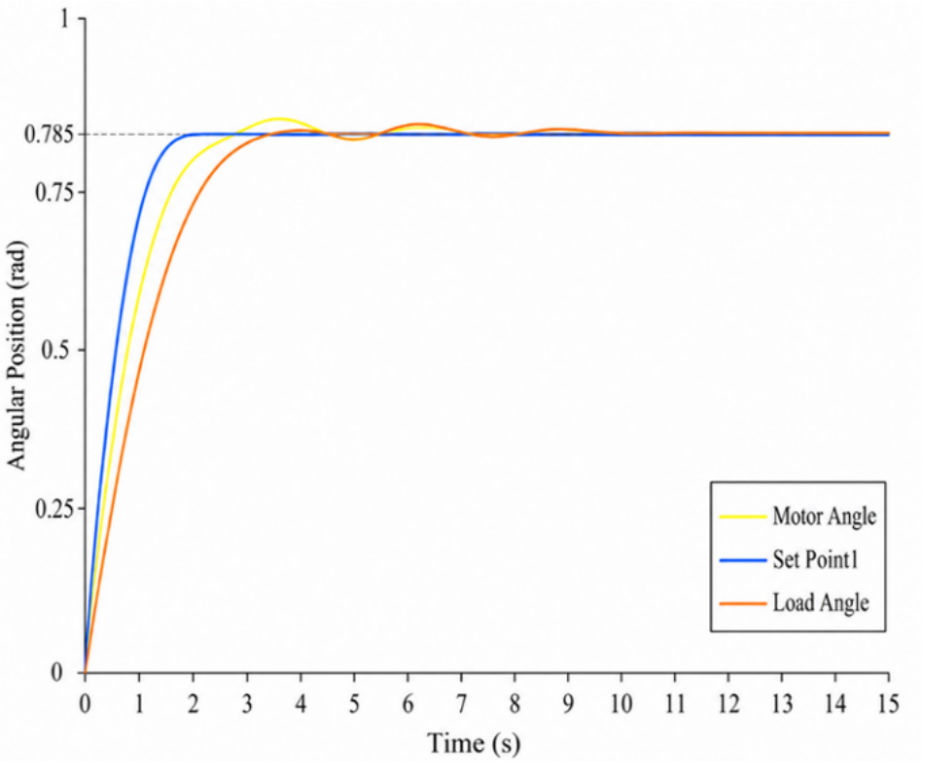


Figure 19. *Experimental Response Of The ASMC Controller Under The No-load Condition*

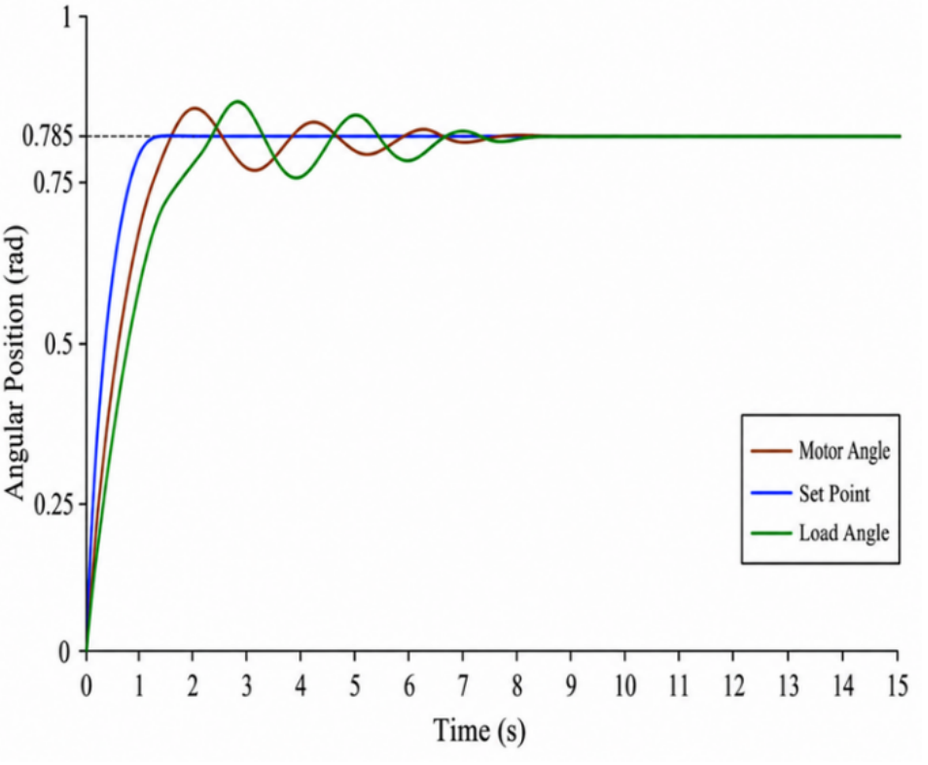


Figure 20. *Motor And Load Angular Positions With A 1000 g Payload At A* 45° *Set Point*

The corresponding ASMC disturbance case is presented in Figure 21. The reported load-side response shows a temporary deviation followed by diminishing oscillation and recovery toward the command. Table 5 summarizes the supplied ASMC performance values for the investigated operating conditions. The table permits a matched numerical comparison with SMC, but the account does not specify repeat counts or variability among trials. The results therefore describe the reported test outcomes rather than a statistical estimate of average performance or a guaranteed worst-case response.

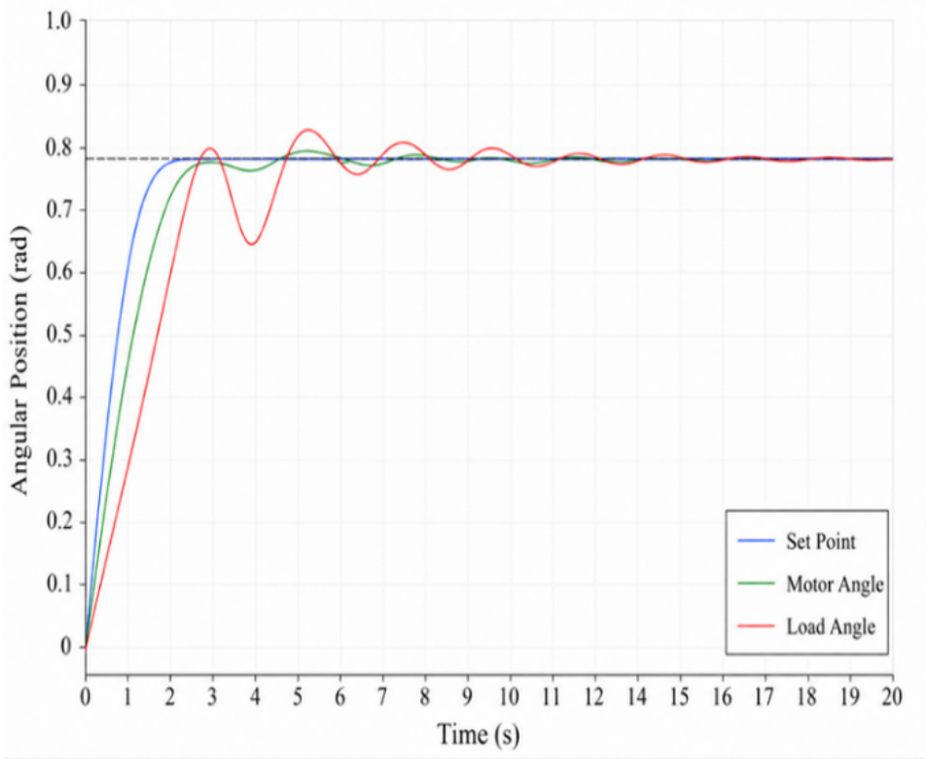


Figure 21. *Experimental Response Of The ASMC With A 1000 g Load And An External Disturbance*

Table 5. *Experimental Performance Of ASMC Under Different Operating Conditions*

Reference Angle	Operating Condition	Settling Time (s)	Position Error (%)	Maximum Load Torque (N m)
45°	No-load	5.5	0.62	3.14
45°	1000 g Payload	5.7	0.82	3.28
45°	External Disturbance	5.9	1.04	3.45
135°	No-load	5.6	0.58	3.85
135°	1000 g Payload	5.9	0.82	5.05
135°	External Disturbance	6.2	1.18	5.45

Tables 4 and 5 contain the experimental SMC and ASMC values, respectively. SMC settling times range from 5.8 to 6.5 s, whereas the corresponding ASMC values range from 5.5 to 6.2 s. SMC position errors range from 1.08 to 2.08%, compared with 0.58 to 1.18% for ASMC. These ranges summarize different operating conditions and should not replace matched comparisons. Table 6 therefore reports a separate reduction for each angle and condition. For any indicator z, the reduction is calculated as $100(z_{\mathrm{SMC}} - z_{\mathrm{ASMC}})/z_{\mathrm{SMC}}$. This is a relative change in the reported indicator, not a percentage-point difference or a significance test. For example, the 45° no-load error changes from 1.12% to 0.62%, giving a relative reduction of 44.6% and an absolute difference of 0.50 percentage points. Both descriptions refer to the same pair of values but convey different quantities.

Table 6. *Relative Reductions In Experimental Performance Indicators For ASMC Compared With SMC*

Reference Angle	Operating Condition	Position Error Reduction (%)	Maximum Load Torque Reduction (%)	Settling Time Reduction (%)
45°	No-load	44.6	35.4	5.2
45°	1000 g payload	42.3	33.3	5.0
45°	External disturbance	50.0	30.3	6.3
135°	No-load	46.3	25.7	5.1
135°	1000 g payload	40.6	13.2	4.8
135°	External disturbance	40.4	11.8	4.6

Reductions are calculated from matched rows of Tables 4 and 5 using the SMC value as the denominator. Values are rounded to one decimal place.

Across the six matched experimental cases, the ASMC values are lower for all three supplied indicators. The position-error reductions range from 40.4 to 50.0%, the maximum-load-torque reductions from 11.8 to 35.4%, and the settling-time reductions from 4.6 to 6.3%. The torque advantage is therefore not approximately 35% in every case; the 135° loaded and disturbed rows show smaller reductions. The calculations in Table 6 follow the supplied measurements rather than

the inconsistent percentages in the original summary. The findings support a restricted statement of improved reported tracking and settling performance for this implementation. They do not isolate adaptation from smoothing or establish a general reduction in actuator energy use.

3.3. INTERPRETATION AND REPORTING LIMITATIONS

The simulation and experimental summaries show broadly similar directional differences between SMC and ASMC, but agreement in trends is weaker evidence than a calibrated model-validation exercise. Position-error definitions, settling bands, torque estimation, synchronization, and disturbance matching affect any comparison. For example, a settling time depends on the tolerance band and the interval over which the response remains inside it. A percentage tracking error depends on the normalization reference and whether the statistic is instantaneous, steady-state, maximum, or averaged. Because those definitions are not fully reported, the values are retained without assigning an undocumented formula to their original measurement.

The supplied platform description also does not specify sensor models, angular resolution, calibration procedures, derivative estimation, sampling interval, software version, communication delays, or actuator command limits. These details can materially affect the apparent smoothness of the response and the implementation of a switching law. The four-spring geometry is described, but its individual spring constants, preload, damping, torque–deflection calibration, and allowable relative rotation are not supplied. Identifying those quantities would connect the fabricated mechanism more directly to the model. No additional measurements or parameter values are inferred from the tables or from a nominal servo rating.

The controller comparison is limited to the two stated implementations. A fixed-gain controller with the same smoothing function would help separate the effect of adaptation from the effect of replacing the sign function. Repeated trials would permit assessment of variability, while RMS torque, integrated energy, or a defined high-frequency metric would address aspects not captured by a maximum load torque. These are potential extensions rather than experiments claimed in this manuscript. Related work on passivity-based, energy-based, and sliding-surface control provides a useful context for evaluating vibration, actuator dynamics, and compliance without assuming that the present controller is superior to methods not tested here [38–41].

4. CONCLUSIONS

This study describes the fabrication, dynamic formulation, simulation, and experimental comparison of a robotic platform incorporating a four-spring flexible coupling. The reported performance values support the following conclusions within the tested operating conditions:

1. The supplied dynamic formulation distinguishes motor-side and load-side motion and includes the spring torque through an explicit distribution vector. Complete numerical reproduction still requires the elastic torque law, model parameters, and a clarified mapping between the four-coordinate representation and the reported hardware degrees of freedom.

2. Both controller implementations are reported to recover toward the reference under no added payload, a 1000 g payload, and an external disturbance. These finite-test responses support a comparison of the observed cases, but they are not a general proof of stability for all operating conditions.

3. Across the six matched experimental rows, ASMC reduces the reported position-error indicator by 40.4–50.0%, maximum load torque by 11.8–35.4%, and settling time by 4.6–6.3%. The reductions vary with reference angle and operating condition, so a single percentage does not characterize every result.

4. The adaptive controller combines gain adaptation with a smooth hyperbolic-tangent switching term. The reported response is described as less oscillatory, but the summary data do not establish complete elimination of chattering or identify the separate contribution of each controller modification.

5. The four-spring mechanism provides a fabricated platform for investigating elastic motor–load interaction. Its reported tracking performance motivates further characterization of the torque–deflection relation, spring parameters, actuator limitations, and the relationship between mechanical compliance and controlled positioning.

6. Further work should provide the complete numerical model, controller settings, signal processing details, disturbance protocol, and repeated time-series measurements. Those additions would support a more reproducible assessment of model agreement, experimental variability, control effort, and the theoretical conditions associated with the reported implementations.

Author Contributions

Both authors contributed equally to this study. They participated in preparing and reviewing the manuscript and approved its final version for publication.

Conflict Of Interest

The authors declare no conflicts of interest.

Funding

This research received no external funding.

Data Availability Statement

The summary simulation and experimental performance values used in the comparative calculations are provided in the tables within this article. No public repository for the underlying time-series measurements, model files, or controller implementation is identified in the supplied materials.

REFERENCES

[1] Wang, Jing; Zhou, Shisheng; Wu, Jimei; Qing, Jiajuan; Kang, Tuo; Shao, Mingyue. "Dynamic Modeling and Analysis of Flexible-Joint Robots with Clearance." *Sensors*, vol. 24, no. 13, 2024, article 4396. https://doi.org/10.3390/s24134396.

[2] Hua, Tuan Minh; Sanfilippo, Filippo; Nguyen, Vinh Hao. "Modelling and Control of a 2-DOF Robot Arm with Elastic Joints for Safe Human-Robot Interaction." *Frontiers in Robotics and AI*, vol. 8, 2021, article 679304. https://doi.org/10.3389/frobt.2021.679304.

[3] van Ommeren, Christiaan. *Analysis and Control of Flexible-Joint Lightweight Robots*. Master's thesis, Technical University of Munich, 2022, 87 pp. DLR institutional record: https://elib.dlr.de/189531/.

[4] Iskandar, Maged; van Ommeren, Christiaan; Wu, Xuwei; Albu-Schaffer, Alin; Dietrich, Alexander. "Model Predictive Control Applied to Different Time-Scale Dynamics of Flexible Joint Robots." *IEEE Robotics and Automation Letters*, vol. 8, no. 2, 2023, pp. 672–679. https://doi.org/10.1109/lra.2022.3229226.

[5] Keppler, Manuel; Lakatos, Dominic; Ott, Christian; Albu-Schaffer, Alin. "Elastic Structure Preserving (ESP) Control for Compliantly Actuated Robots." *IEEE Transactions on Robotics*, vol. 34, no. 2, 2018, pp. 317–335. https://doi.org/10.1109/tro.2017.2776314.

[6] Moyrón, Jerónimo; Ott, Christian; Kirner, Annika; Moreno-Valenzuela, Javier. "Elastic Structure Preserving Control for Flexible Joint Robots With Position-Controlled Actuators." *IEEE Transactions on Control Systems Technology*, vol. 33, no. 5, 2025, pp. 1810–1819. https://doi.org/10.1109/tcst.2025.3562024.

[7] Buondonno, Gabriele; De Luca, Alessandro. "A recursive Newton-Euler algorithm for robots with elastic joints and its application to control." *Proceedings of the 2015 IEEE/RSJ International Conference on Intelligent Robots and Systems (IROS)*, 2015, pp. 5526–5532. https://doi.org/10.1109/iros.2015.7354160.

[8] Shang, Dongyang; Li, Xiaopeng; Yin, Meng; Li, Fanjie. "Dynamic modeling and fuzzy adaptive control strategy for space flexible robotic arm considering joint flexibility based on improved sliding mode controller." *Advances in Space Research*, vol. 70, no. 11, 2022, pp. 3520–3539. https://doi.org/10.1016/j.asr.2022.08.042.

[9] Ruderman, Michael. "Compensation of Nonlinear Torsion in Flexible Joint Robots: Comparison of Two Approaches." *IEEE Transactions on Industrial Electronics*, vol. 63, no. 9, 2016, pp. 5744–5751. https://doi.org/10.1109/tie.2016.2574299.

[10] Zhang, Qi; Xie, Zongwu; Liu, Hong; Cai, Hegao. "Flexible Joint Controller Design Based on Passivity Theory." *Robot*, vol. 35, no. 1, 2013, pp. 23–31. https://doi.org/10.3724/sp.j.1218.2013.00023.

[11] Spong, M. W.. "Modeling and Control of Elastic Joint Robots." *Journal of Dynamic Systems, Measurement, and Control*, vol. 109, no. 4, 1987, pp. 310–318. https://doi.org/10.1115/1.3143860.

[12] Xu, Xinglei; Xu, Shiwei. "Event-Triggered Adaptive Neural Tracking Control of Flexible-Joint Robot Systems With Input Saturation." *IEEE Access*, vol. 10, 2022, pp. 43367–43375. https://doi.org/10.1109/access.2022.3169012.

[13] Ma, Hui; Zhou, Qi; Li, Hongyi; Lu, Renquan. "Adaptive Prescribed Performance Control of A Flexible-Joint Robotic Manipulator With Dynamic Uncertainties." *IEEE Transactions on Cybernetics*, vol. 52, no. 12, 2022, pp. 12905–12915. https://doi.org/10.1109/tcyb.2021.3091531.

[14] Qi, Rui; Lam, Hak-Keung; Liu, Jiapeng; Yu, Jinpeng. "Adaptive Fuzzy Finite-Time Singular Perturbation Control for Flexible Joint Manipulators With State Constraints." *IEEE Transactions on Systems, Man, and Cybernetics: Systems*, vol. 54, no. 12, 2024, pp. 7521–7527. https://doi.org/10.1109/tsmc.2024.3446172.

[15] Pan, Changzhong; Fei, Xiangyin; Xiao, Jinsen; Xiong, Peiyin; Li, Zhijing; Huang, Hao. "Model-Assisted Reduced-Order ESO Based Command Filtered Tracking Control of Flexible-Joint Manipulators with Matched and Mismatched Disturbances." *Applied Sciences*, vol. 12, no. 17, 2022, article 8511. https://doi.org/10.3390/app12178511.

[16] Cao, Shiqi; Wang, Fan; Li, Xin; Yao, Dalei; Xie, Meilin. "Safety-Constrained Disturbance-Compensated Model Predictive Control for Flexible-Joint Robots." *Applied Sciences*, vol. 15, no. 24, 2025, article 13238. https://doi.org/10.3390/app152413238.

[17] Lee, Sang-Hun; Hur, Jong-Sung; Cho, Hyun-Chul; and Park, Jong-Hyeon. "A PID-Type Robust Controller Design for Industrial Robots with Flexible Joints." *Proceedings of the SICE-ICASE International Joint Conference*, IEEE, 2006, pp. 5905–5910. Conference program: https://icros.org/convention/SICE-ICCAS2006_toc.pdf.

[18] Sun, Lei; Yin, Wei; Wang, Meng; Liu, Jingtai. "Position Control for Flexible Joint Robot Based on Online Gravity Compensation With Vibration Suppression." *IEEE Transactions on Industrial Electronics*, vol. 65, no. 6, 2018, pp. 4840–4848. https://doi.org/10.1109/tie.2017.2772157.

[19] Pham, Minh-Nha; Hamelin, Philippe; Hazel, Bruce; Liu, Zhaoheng. "A Two-Stage State Feedback Controller Supported by Disturbance-State Observer for Vibration Control of a Flexible-Joint Robot." *Robotica*, vol. 38, no. 6, 2020, pp. 1082–1104. https://doi.org/10.1017/s0263574719001267.

[20] Cheng, Xin; Zhang, Yajun; Liu, Huashan; Wollherr, Dirk; Buss, Martin. "Adaptive neural backstepping control for flexible-joint robot manipulator with bounded torque inputs." *Neurocomputing*, vol. 458, 2021, pp. 70–86. https://doi.org/10.1016/j.neucom.2021.06.013.

[21] Li, Jian; Ma, Kaifa; Wu, Zhaojing. "Prescribed Performance Control for Uncertain Flexible-joint Robotic Manipulators Driven by DC Motors." *International Journal of Control, Automation and Systems*, vol. 19, no. 4, 2021, pp. 1640–1650. https://doi.org/10.1007/s12555-020-0311-2.

[22] Liu, Huashan; Huang, Yong. "Robust adaptive output feedback tracking control for flexible-joint robot manipulators based on singularly perturbed decoupling." *Robotica*, vol. 36, no. 6, 2018, pp. 822–838. https://doi.org/10.1017/s0263574718000061.

[23] Rsetam, Kamal; Cao, Zhenwei; Man, Zhihong. "Design of Robust Terminal Sliding Mode Control for Underactuated Flexible Joint Robot." *IEEE Transactions on Systems, Man, and Cybernetics: Systems*, vol. 52, no. 7, 2022, pp. 4272–4285. https://doi.org/10.1109/tsmc.2021.3096835.

[24] Wang, Huiming; Zhang, Qiyao; Sun, Zhenxing; Tang, Xianlun; Chen, I-Ming. "Continuous Terminal Sliding-Mode Control for FJR Subject to Matched/Mismatched Disturbances." *IEEE Transactions on Cybernetics*, vol. 52, no. 10, 2022, pp. 10479–10489. https://doi.org/10.1109/tcyb.2021.3066593.

[25] Cheng, Xin; Liu, Huashan; Lu, Wenke. "Chattering-Suppressed Sliding Mode Control for Flexible-Joint Robot Manipulators." *Actuators*, vol. 10, no. 11, 2021, article 288. https://doi.org/10.3390/act10110288.

[26] Zaare, Saeed; Soltanpour, Mohammad Reza. "Adaptive fuzzy global coupled nonsingular fast terminal sliding mode control of n-rigid-link elastic-joint robot manipulators in presence of uncertainties." *Mechanical Systems and Signal Processing*, vol. 163, 2022, article 108165. https://doi.org/10.1016/j.ymssp.2021.108165.

[27] Al-Ashtari, Waleed; Ali, Karim H.. "Design of a Hybrid Adaptive Controller for Series Elastic Actuators of Robots." *Journal Européen des Systèmes Automatisés*, vol. 56, no. 6, 2023, pp. 1053–1063. https://doi.org/10.18280/jesa.560615.

[28] Zotovic-Stanisic, Ranko; Perez-Ubeda, Rodrigo; Perles, Angel. "Comparative Study of Methods for Robot Control with Flexible Joints." *Actuators*, vol. 13, no. 8, 2024, article 299. https://doi.org/10.3390/act13080299.

[29] Moyrón, Jerónimo; Moreno–Valenzuela, Javier; Sandoval, Jesús. "Nonlinear PI"D"-Type Control of Flexible Joint Robots by Using Motor Position Measurements Is Globally Asymptotically Stable." *IEEE Transactions on Automatic Control*, vol. 68, no. 6, 2023, pp. 3648–3655. https://doi.org/10.1109/tac.2022.3194043.

[30] Amaini, Rafik; Ferguene, Farid. "Hybrid force/position approach for flexible-joint robot with fuzzy-super twisting sliding mode control." *IAES International Journal of Robotics and Automation (IJRA)*, vol. 15, no. 1, 2026, pp. 21–32. https://doi.org/10.11591/ijra.v15i1.pp21-32.

[31] Siciliano, Bruno; Sciavicco, Lorenzo; Villani, Luigi; and Oriolo, Giuseppe. *Robotics: Modelling, Planning and Control*. London: Springer, 2009. https://doi.org/10.1007/978-1-84628-642-1.

[32] Slotine, Jean-Jacques E.. "Sliding controller design for non-linear systems." *International Journal of Control*, vol. 40, no. 2, 1984, pp. 421–434. https://doi.org/10.1080/00207178408933284.

[33] Edwards, Christopher, and Sarah K. Spurgeon. *Sliding Mode Control: Theory and Applications*. London: Taylor & Francis, 1998. ISBN 9780748406012. https://www.routledge.com/Sliding-Mode-Control-Theory-And-Applications/Edwards-Spurgeon/p/book/9780748406012.

[34] Alqaisi, Walid Kh.; Soliman, Mostafa; Badawi, Ahmed; Elzein, I. M.; El-Bayeh, Claude Ziad. "Four DOF Robot Manipulator Control Using Feedback Linearization Based on Sliding Mode Control." *International Journal of Robotics and Control Systems*, vol. 5, no. 2, 2025, pp. 781–793. https://doi.org/10.31763/ijrcs.v5i2.1729.

[35] Khalil, Hassan K. *Nonlinear Systems*. 3rd ed. Upper Saddle River, NJ: Prentice Hall, 2002. ISBN 9780130673893.

[36] Baek, Seungmin; Baek, Jaemin; Han, Soohee. "An Adaptive Sliding Mode Control With Effective Switching Gain Tuning Near the Sliding Surface." *IEEE Access*, vol. 7, 2019, pp. 15563–15572. https://doi.org/10.1109/access.2019.2894911.

[37] Shtessel, Yuri; Edwards, Christopher; Fridman, Leonid; and Levant, Arie. *Sliding Mode Control and Observation*. New York: Birkhäuser, 2014. https://doi.org/10.1007/978-0-8176-4893-0.

[38] Ott, C.; Albu-Schaffer, A.; Kugi, A.; Hirzinger, G.. "On the Passivity-Based Impedance Control of Flexible Joint Robots." *IEEE Transactions on Robotics*, vol. 24, no. 2, 2008, pp. 416–429. https://doi.org/10.1109/tro.2008.915438.

[39] Albu-Schäffer, Alin; Ott, Christian; Hirzinger, Gerd. "A Unified Passivity-based Control Framework for Position, Torque and Impedance Control of Flexible Joint Robots." *The International Journal of Robotics Research*, vol. 26, no. 1, 2007, pp. 23–39. https://doi.org/10.1177/0278364907073776.

[40] Yin, Wei; Sun, Lei; Wang, Meng; Liu, Jingtai. "Nonlinear state feedback position control for flexible joint robot with energy shaping." *Robotics and Autonomous Systems*, vol. 99, 2018, pp. 121–134. https://doi.org/10.1016/j.robot.2017.10.007.

[41] Slotine, J. J.; Sastry, S. S.. "Tracking control of non-linear systems using sliding surfaces, with application to robot manipulators." *International Journal of Control*, vol. 38, no. 2, 1983, pp. 465–492. https://doi.org/10.1080/00207178308933088.